



Effect of TiO₂ nanoshape on the photoproduction of hydrogen from water-ethanol mixtures over Au₃Cu/TiO₂ prepared with preformed Au-Cu alloy nanoparticles



Lester Martínez^a, Lluís Soler^{a,*}, Inmaculada Angurell^b, Jordi Llorca^{a,*}

^a Institute of Energy Technologies, Department of Chemical Engineering and Barcelona Research Center in Multiscale Science and Engineering, Universitat Politècnica de Catalunya, EEBE, Eduard Maristany 16, 08019 Barcelona, Spain

^b Departament de Química Inorgànica i Òrgànica, Secció de Química Inorgànica, Universitat de Barcelona, Martí i Franquès, 1-11, 08028 Barcelona, Spain

ARTICLE INFO

Keywords:
Photocatalysis
Titanium dioxide
Nanoshapes
Au-Cu nanoparticles
Hydrogen

ABSTRACT

A series of TiO₂ nanoshapes (microurchins, nanobelts, nanowires, microrods and nanotubes) were prepared and decorated with preformed nanoparticles of Au-Cu alloy (Au:Cu = 3:1 molar, 1 wt.% metal content). The resulting photocatalysts were tested for the photogeneration of hydrogen using water-ethanol gaseous mixtures (H₂O:EtOH = 1:9 molar basis) under dynamic conditions (26,000 h⁻¹) and compared with a conventional sample prepared using P25. The use of preformed nanoparticles of Au-Cu alloy with the same geometric and electronic characteristics ensured a proper assessment of the influence of the different TiO₂ supports on the photoproduction of hydrogen by providing a similar number and quality of metal-support contact points. The yield of hydrogen produced on a weight basis over the Au₃Cu/TiO₂ samples followed the trend microrods ~P25 > nanotubes > nanowires > nanobelts > microurchins. A stable hydrogen photogeneration rate of ca. 270 μmol H₂ g⁻¹ min⁻¹ was obtained over titania microrods decorated with Au₃Cu whereas the photogeneration of hydrogen over P25 decorated with Au₃Cu decreased progressively over time on stream.

1. Introduction

The photocatalytic production of hydrogen is one of the most sustainable processes to obtain renewable hydrogen, which is a powerful energy carrier that, combined with fuel cells, can help us to manage and store energy in a very efficient way. Upon light irradiation, electrons and holes accumulate on the surface of the photocatalyst and H₂ can be obtained when these electrons reduce hydrogen ions [1]. Among the photocatalysts tested so far for hydrogen generation, TiO₂-based materials are the most widely used due to a proper balance between photocatalytic activity, low cost, availability and stability [2]. Recently, the use of 1D, 2D and 3D nanostructured TiO₂ has attracted interest to improve the photocatalytic performance and several works have been reported in the literature showing the beneficial effect of controlling the dimensionality and architecture of TiO₂ for the photoproduction of hydrogen [3–10]. To that end, different synthetic procedures, such as electrochemical anodization [11–13], atomic layer deposition [14], microwave-assisted synthesis [15,16], flame synthesis [17], solvothermal methods [18–21] and hydrothermal methods [22–28] have been used to fabricate diverse types of micro- and nanoshaped TiO₂.

However, some of these methods are complex and include multiple steps or expensive equipment and reagents [29–31]. Among the above-mentioned methods, the hydrothermal route is the most used one since it has many advantages, such as simplicity, scalability and cost-effectiveness. Nevertheless, the hydrothermal methods used to produce 1D TiO₂ nanostructures as nanotubes, nanowires and nanobelts present the inconvenience of requiring an acid treatment step and intensive washing, which are time-consuming and may generate a great variability in the characteristics and properties of the resulting materials [32,33]. In addition, hydrothermal methods usually require long reaction times (up to 72 h). Therefore, the development of synthetic methods of nanoshaped TiO₂ with an improved efficiency and a short preparation time is highly desirable. In this work, we have used for the first time (to the best of our knowledge) TiO₂ microrods for the photogeneration of hydrogen, which can be obtained at short reaction times by simple methods. We compare the photocatalytic efficiency of this material containing preformed Au₃Cu nanoparticles to generate hydrogen from water-ethanol mixtures under dynamic gas-phase conditions against well-known nanoshaped TiO₂ nanobelts, nanotubes, nanowires and urchins as well as standard P25.

* Corresponding authors.

E-mail addresses: lluis.soler.turu@upc.edu (L. Soler), jordi.llorca@upc.edu (J. Llorca).

It is important to highlight that neither the shape and dimensions of the metal nanoparticles nor the architecture of the metal-TiO₂ interaction are comparable when the metal nanoparticles are synthesized by conventional impregnation or photoreduction methods [1,34–36]. The use of preformed nanoparticles guarantees the same metal particle size and a similar architecture of the Au-Cu/TiO₂ interphase for all the samples tested. Here we have deposited the metal nanoparticles on the different TiO₂ shaped materials in a way that the characteristics of the metal nanoparticles are common over all the photocatalysts. In this way, the effect of the shape of the support can be precisely evaluated. This approach has been used successfully, for instance, in deciphering the role of nanoshaped CeO₂ (nanocubes, nanorods and nanopolyhedra) in the oxidation of CO over Au/CeO₂ catalysts [37]. Here we have chosen bimetallic nanoparticles of Au-Cu alloy with a Au₃Cu composition since they have shown an excellent performance in the photo-production of hydrogen from water-ethanol mixtures in previous experiments using standard TiO₂ decorated with bimetallic nanoparticles with different Au:Cu ratios [38]. Non-noble metal Cu not only facilitates the separation of carriers, but also reduces the overpotential of hydrogen evolution, thus promoting the photocatalytic activity for H₂ production [39,40].

2. Experimental section

2.1. Materials

Commercial TiO₂ (P25 ca. 80% anatase and 20% rutile, purity > 99.55%) was purchased from Evonik; sodium hydroxide (NaOH), potassium hydroxide (KOH) and ethylene glycol ((CH₂OH)₂) were purchased from Fisher Scientific; hydrochloric acid (HCl) and titanium(IV) n-butoxide (Ti(OBuⁿ)₄, 97%) were purchased from Sigma-Aldrich; absolute ethanol was purchased from Scharlau. All reagents were used without further purification.

2.2. Preparation of TiO₂ nanotubes, TiO₂ nanobelts and TiO₂ nanowires

For the synthesis of TiO₂ nanotubes, nanobelts and nanowires, sodium titanate nanotubes, nanobelts and nanowires were first prepared by alkaline hydrothermal treatment of P25 TiO₂ powder according to the method described by Kasuga et al. [41]. In a typical synthesis, about 3.5 g of TiO₂ P25 was added into 280 mL of a 10 M NaOH or KOH aqueous solution. After stirring for 1 h at room temperature, the white suspension was transferred into a 300 mL Teflon-lined autoclave, which was heated at 403–473 K for 20–42 h. Table 1 compiles the exact synthesis conditions used for the preparation of each nanoshape. The white precipitate of sodium titanate formed in the hydrothermal synthesis was collected by centrifugation, washed repeatedly with

Table 1
Synthetic conditions used for the preparation of nanoshaped titania samples.

Shape	abbreviation	Reaction medium	Ratio (g/L) ^a	Reaction temperature (K) and time	Calcination temperature (K) and time
TiO ₂ prepared by hydrothermal methods					
Nanotubes	Ti-NT	NaOH 10 M	12.5	403 (42 h)	673 (2 h)
Nanobelts	Ti-NB	NaOH 10 M	12.5	453 (20 h)	773 (5 h)
Nanowires	Ti-NW	KOH 10 M	14	473 (24 h)	773 (2 h)
Urchins	Ti-MU	HCl 5.5 M	100	463 (4 h)	–
TiO ₂ prepared by polyol method					
Microrods	Ti-MR	Ethylene glycol	10	443 (2 h)	673 (4 h)

^a grams of precursor per liter of solution employed.

deionized water until the pH of the waste washing liquid was near 7, and finally dried at 353 K for 10 h. Hydrogen titanate nanotubes, nanobelts and nanowires were prepared by placing the corresponding sodium titanate nanoshape in contact with a 0.5 M HCl aqueous solution and stirring the mixture for 7 h. The hydrogen titanate nanoshapes were collected by centrifugation, washed with deionized until pH~7, dried at 353 K overnight and finally calcined at 673–773 K (2 K min⁻¹) for 2–5 h to obtain the corresponding TiO₂ nanotubes, nanobelts and nanowires. The calcination conditions for each nanoshaped TiO₂ support are summarized in Table 1 as well as the abbreviations used in this work.

2.3. Preparation of TiO₂ urchins

Urchin-like TiO₂ microspheres were prepared following the procedure described in [42]. Titanium(IV) n-butoxide was diluted to a final concentration of 0.29 M in 60 mL of 5.5 M HCl solution. After stirring for 30 min, the solution was put into a Teflon-lined stainless steel autoclave and heated at 463 K for 4 h. The resulting solid was washed with ethanol, dried at 353 K for 24 h and used without any further treatment.

2.4. Preparation of TiO₂ microrods

TiO₂ microrods were prepared by the polyol method following the protocol described in [43]. Briefly, 2.5 mL of titanium(IV) n-butoxide were mixed with 250 mL of ethylene glycol. The solution was stirred for 1 h and heated at 443 K for 2 h. The resulting precipitate was washed with water, dried at 353 K overnight and calcined at 673 K (2 K min⁻¹) for 4 h.

2.5. Preparation of Au₃Cu/TiO₂ photocatalysts

Bimetallic Au-Cu nanoparticles encapsulated with dodecanethiol monolayer shells were synthesized according to the two-phase method described for the synthesis of dodecanethiol-capped monometallic Au nanoparticles [44,45] and metal alloys [46]. The Au:Cu atomic ratio was fixed at 3:1 following previous reports [38]. The size of the as-prepared Au-Cu nanoparticles was determined by TEM to be 2.2 ± 0.3 [47]. The Au-Cu nanoparticles were suspended in toluene and impregnated onto each TiO₂ nanostructure by incipient wetness impregnation. The nominal Au-Cu loading was 1 wt.% with respect to TiO₂. This metal loading was determined as an optimum value in previous studies [48]. To ensure the same metal loading over the different TiO₂ supports, equal aliquots from a single toluene suspension were used with an automatic micropipette. Samples were dried at 353 K for 24 h and calcined at 573 K (2 K min⁻¹) for 4 h to eliminate the dodecanethiol shell and to assure a strong contact between the bimetallic nanoparticles and the TiO₂ supports as reported elsewhere [47]. The resulting photocatalysts were labeled as AuCu/Ti-NT, AuCu/Ti-NB, AuCu/Ti-NW, AuCu/Ti-MU, and AuCu/Ti-MR and correspond to Au₃Cu nanoparticles anchored on TiO₂ nanotubes, nanobelts, nanowires, urchins and microrods, respectively. For comparative purposes, conventional titania P25 was also impregnated with Au-Cu nanoparticles and calcined following exactly the same procedure. The resulting sample was labeled as AuCu/Ti-P25. The elemental composition of the resulting samples was analyzed by ICP-OES.

2.6. Characterization

Scanning electron microscopy (SEM) images were recorded at 5 kV using a Zeiss Neon40Crossbeam Station instrument equipped with a field emission source. Microstructural characterization by high resolution transmission electron microscopy (HRTEM) was performed at an accelerating voltage of 200 kV in a JEOL 2010 F instrument equipped with a field emission source. The point-to-point resolution was 0.19 nm and the resolution between lines was 0.14 nm. Samples were dispersed

in alcohol in an ultrasonic bath, and a drop of supernatant suspension was poured onto a holey carbon-coated grid. X-ray diffraction (XRD) analysis was performed using a Bruker D8 diffractometer with Cu K α radiation (40 mA, 40 kV). X-ray photoelectron spectroscopy (XPS) was carried out on a SPECS system equipped with an Al anode XR50 source operating at 150 mW and a Phoibos MCD-9 detector. The pass energy of the hemispherical analyzer was set at 25 eV and the energy step was set at 0.1 eV. Data processing was performed with the CasaXPS program (Casa Software Ltd., UK). Atomic fractions were calculated using peak areas normalized on the basis of acquisition parameters after subtraction of the background, experimental sensitivity factors and transmission factors provided by the manufacturer. Raman spectroscopy was performed over the range of 50 to 800 cm $^{-1}$ on a Renishaw inVia Qontor confocal Raman microscope using a laser excitation source of 532 nm directed to the sample through a Leica DM2700 M microscope. The scattered light was collected and directed to the CCD detector of the Raman spectrometer with a grating of 2400 lines mm $^{-1}$. The power of the laser at the sample was kept below 5 mW cm $^{-2}$. UV-vis reflectance spectroscopy was performed on a Shimadzu UV3600 UV-vis/NIR apparatus equipped with a diffuse reflectance cell and using BaSO₄ as reference standard. Surface area measurements (BET method) were carried out with a Micromeritics ASAP2020 gas adsorption instrument. The materials were degassed at 500 °C for 10 h prior to the adsorption experiments. Inductively Coupled Plasma Optical Emission Spectrometry (ICP-OES) was carried out using an Agilent 5100 instrument.

2.7. Photocatalytic experiments

A controlled amount of the photocatalyst (between 0.5 and 7 mg) was dispersed in ethanol and exposed to ultrasonication to obtain an homogeneous suspension, which was poured onto a circular porous cellulose membrane (Albet, pore size 35–40 μm, 80 g m $^{-2}$, thickness 0.18 mm) forming a circle of supported photocatalyst of 1.8 cm in diameter. The impregnated membrane was dried at 323 K for 1 h. The photocatalytic tests were performed with the impregnated membrane at room temperature and atmospheric pressure in a tubular glass photoreactor [49]. An argon stream was bubbled through a Drechsel bottle containing a liquid mixture of ethanol-water in order to obtain a gaseous reactant mixture of EtOH:H₂O = 1:9 (molar), which was directly introduced in the photoreactor and forced to pass through the impregnated membrane at a gas hourly space velocity (GHSV) of ca. 26,000 h $^{-1}$. An UV-light source (from SACOPA, S.A.U.) consisting of four LEDs emitting at 365 ± 5 nm was aligned to a synthetic quartz glass cylindrical lens to transmit the light towards the photocatalyst. An irradiance of 82 mW cm $^{-2}$ at the position of the photocatalyst was measured with a UVA sensor (model PMA 2110, Solar Light Co.), which registers the UV radiation within a spectral response of 320–400 nm, connected to a radiometer (model PMA2200, Solar Light Co.). The outlet of the photoreactor was connected to a GC (micro gas chromatograph Agilent 490) equipped with MS 5 Å, Plot U and Stabilwax columns for a complete analysis of the photoreaction products, which were monitored on-line every 4 min.

3. Results and discussion

3.1. Characterization

The nanoshaped titania supports were characterized by X-ray diffraction, Raman spectroscopy, scanning electron microscopy and UV-vis spectroscopy and their surface area was determined by BET measurements. Additionally, the AuCu/TiO₂ photocatalysts were also characterized by high-resolution transmission electron microscopy, Raman spectroscopy, UV-vis spectroscopy and X-ray photoelectron spectroscopy. Fig. 1 shows the XRD patterns of the different nanoshaped titania supports prepared in this work. The diffraction peaks

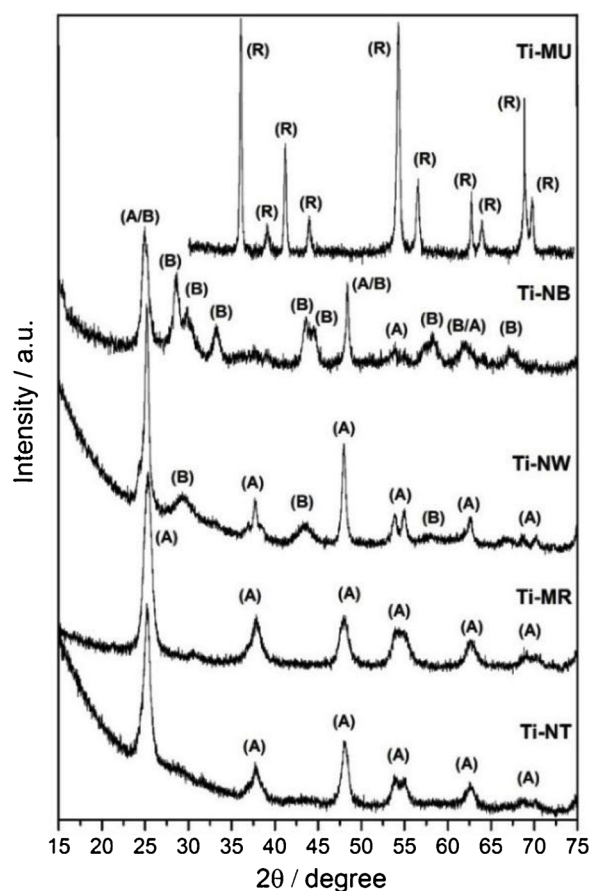


Fig. 1. XRD patterns of the TiO₂ supports prepared in this work.

corresponding to titania nanotubes and titania microrods indicate that these samples are constituted by crystalline anatase, with a mean crystallite size (Scherrer method) of about 11 and 8 nm, respectively (Table 2). The presence of the anatase polymorph in these samples is in accordance to other works that used the same preparation method [43,50]. Regarding the sample of titania microrods, there is a trace signal at about 31° which may correspond to brookite. The XRD pattern of the titania nanowires shows, in addition to anatase, the presence of the TiO_2 (B) polymorph with a mean crystallite size of about 20 nm. The same mixture is identified in the XRD pattern of the titania nanobelts, but in this case the TiO_2 (B) polymorph is dominant, which exhibits a crystallite size of ca. 21 nm. The existence of the TiO_2 (B) polymorph in these samples is also in accordance to works reported by others that used similar hydrothermal preparation methods [51,52]. The XRD profile of the titania urchins clearly show peaks corresponding solely to the rutile polymorph with a mean particle size of ca. 27 nm.

The same polymorph distribution was obtained from Raman spectroscopy (Fig. 2a), which is not limited to crystallinity as it occurs with XRD, and suggests that all the titania samples are totally crystalline. In titania nanotubes and microrods only bands corresponding to anatase at 144, 197, 399, 513, 519 and 639 cm $^{-1}$ were present [53,54], whereas in titania urchins the bands at 115, 143, 235, 445 and 610 cm $^{-1}$ corresponded to pure rutile [53,55]. The spectra of titania nanowires and nanobelts was more complex, with contributions from both anatase and TiO_2 (B) polymorphs. In addition to the bands corresponding to anatase, new bands at 121, 237, 250, 294, 365, 431, 468, 552 and 655 cm $^{-1}$ were present, which are ascribed to the TiO_2 (B) polymorph [56]. Since it is difficult to obtain a reliable estimation of the amount of the different TiO₂ polymorphs present in the samples from XRD data when anatase is in low quantities in anatase-TiO₂(B) mixtures, the Beuvier equation has been used to obtain an estimation of the amount of each

Table 2Crystalline structure, dimensions, surface area and band gap of the nanoshaped titania supports and dimensions of Au₃Cu nanoparticles in AuCu/TiO₂ photocatalysts.

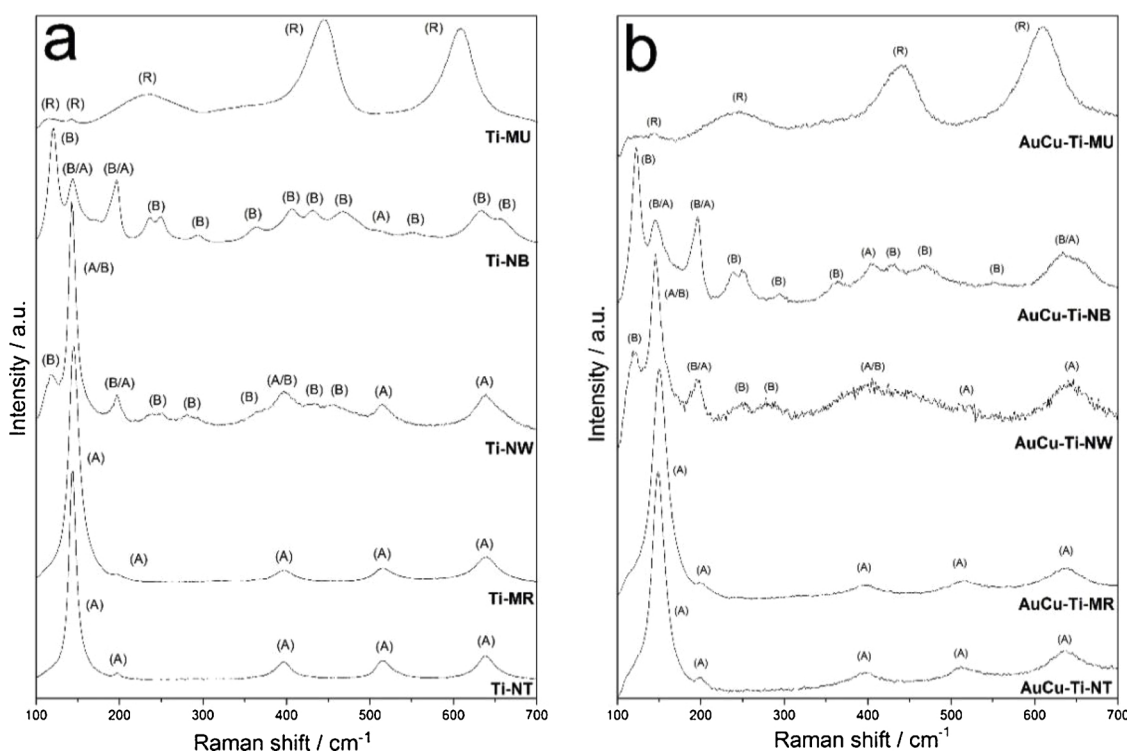
Sample	TiO ₂ dimensions ^a	Crystalline structure ^b	Surface area (m ² g ⁻¹) ^c	AuCu φ (nm) ^d	Elemental composition ^e		Band gap (eV) ^f
					Au	Cu	
AuCu/Ti-NT	L = 0.1–1 μm φ = 10 nm	Anatase	274	5.0 ± 0.4	0.74	0.08	3.32
AuCu/Ti-NB	L = 0.5–2 μm W = 20–100 nm	Anatase (9) TiO ₂ (B) (91)	35	5.0 ± 0.3	0.78	0.09	3.31
AuCu/Ti-NW	L = 0.1–10 μm φ < 10 nm	Anatase (75) TiO ₂ (B) (25)	250	4.9 ± 0.3	0.75	0.08	3.34
AuCu/Ti-MU	L = 2–10 μm φ = 20–50 nm	Rutile	40	4.6 ± 0.6	0.78	0.09	3.06
AuCu/Ti-MR	L = 1–20 μm φ = 1–5 μm	Anatase	61	5.8 ± 0.5	0.74	0.08	3.27

^a measured by SEM.^b measured by XRD and Raman spectroscopy (in parentheses the relative amount of each phase determined by the Beuvier equation is given).^c measured by BET method.^d measured by TEM.^e wt.%, measured by ICP-OES.^f measured by UV-vis from Tauc plots.

polymorph from the Raman spectra [57]. The Beuvier equation is experimental and states that %anatase = y/(6.2–5.2y), where y = I_A/(I_A + I_B), being I_A and I_B the integrated intensities of the main peaks of anatase and TiO₂(B), respectively. The amount of each phase is about anatase:TiO₂(B) = 3:1 for titania nanowires and anatase:TiO₂(B) = 1:9 for titania nanobelts (Table 2). As expected, virtually the same spectra were obtained after deposition of the Au₃Cu preformed nanoparticles (Fig. 2b), except for a slight redshift of the bands corresponding to anatase, as has been already reported to occur for Au nanoparticles supported on anatase [35].

The nanoshape of the TiO₂ supports was confirmed by electron microscopy. Fig. 3 shows representative SEM images under different magnification and the mean dimensions of TiO₂ of each sample are compiled in Table 2. Titania urchins showed a spherical morphology with particles ranging from ca. 5 up to 20 μm in diameter. Within these

particles, the rutile crystals were perfectly radially aligned (Fig. 3a) and measured between 20 and 50 nm in diameter (Fig. 3b). Titania nanobelts occurred as individual particles in the Ti-NB sample (Fig. 3c and d). Their morphology was very homogeneous and the width of the particles was about 20–100 nm and their length ranged mostly between 0.5 and 2 μm. Sample Ti-NW showed a tangled morphology of TiO₂ wires with a diameter below 10 nm. The length of the nanowires varied from about 0.1 up to 10 μm (Fig. 3e and f). Accordingly, the surface areas exhibited by Ti-NB and Ti-NW samples were 35 and 250 m² g⁻¹, respectively (Table 2). Fig. 3g corresponds to a low-magnification image of the Ti-MR sample, which was constituted by well-defined TiO₂ microrods of ca. 1–20 μm in length and a diameter of about 1–5 μm. The surface area of the Ti-MR sample was 61 m² g⁻¹ (Table 2), which is higher than expected taking into account the dimensions of the microrods; however, as shown in Fig. 3h, the surface of the microrods was

**Fig. 2.** Raman spectra of (a) the TiO₂ supports and (b) the AuCu/TiO₂ photocatalysts prepared in this work.

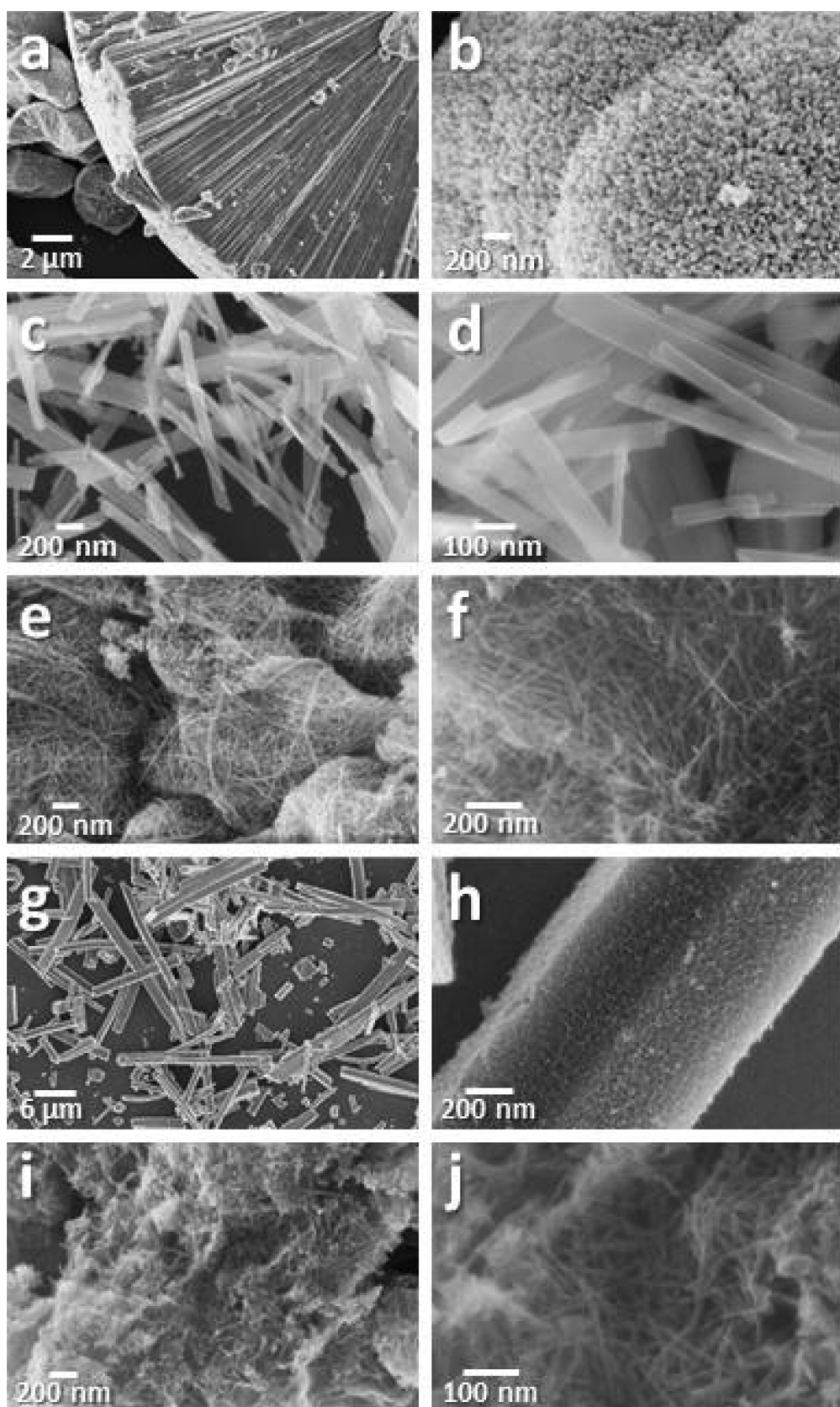


Fig. 3. SEM images of the TiO_2 supports prepared in this work: Ti-MU (a,b), Ti-NB (c,d), Ti-NW (e,f), Ti-MR (g,h) and Ti-NT (i,j).

not smooth, the microrods were decorated by smaller TiO_2 particles, which accounted for a higher surface area exposed than bare microrods. Fig. 3i and j correspond to the sample Ti-NT and show a tangled

morphology of TiO_2 nanotubes. They exhibited a rather homogeneous diameter of about 10 nm and lengths between 100 nm and 1 μm . The surface area measured was $274 \text{ m}^2 \text{ g}^{-1}$ (Table 2).

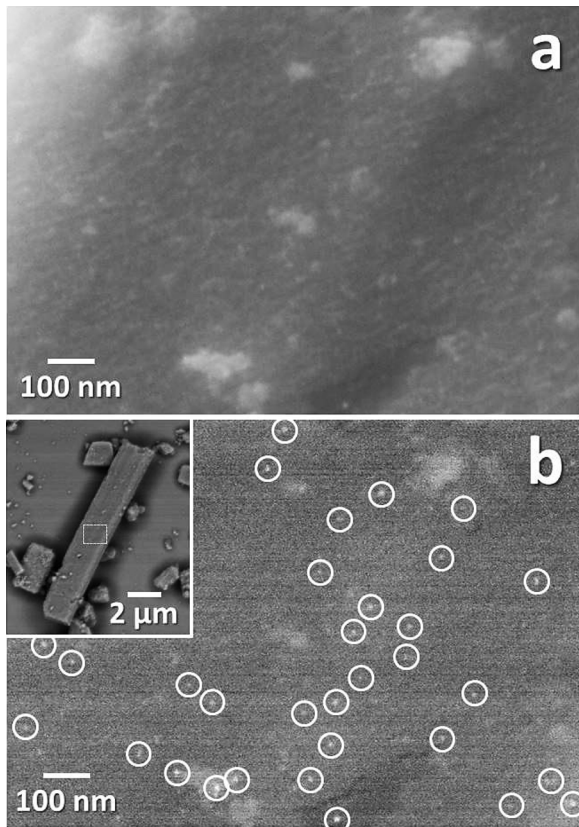


Fig. 4. SEM images of the area enclosed in the white square of a TiO_2 microrod in sample AuCu/Ti-MR (see inset in b) recorded with secondary electrons (a) and backscattered electrons (b). AuCu nanoparticles are inside the white circles in (b).

The nanoshaped titania supports were decorated with preformed Au_3Cu nanoparticles as explained in the experimental section and the resulting AuCu/TiO₂ photocatalysts were characterized by SEM and HRTEM. Given the small size of the AuCu metal nanoparticles, their detailed analysis by SEM was not possible. However, even if SEM was unable to accurately determine the size of the metal nanoparticles, it proved to be useful to study the dispersion of the metal nanoparticles on the titania supports. As an example, Fig. 4 shows representative SEM images of the AuCu/Ti-MR sample. Fig. 4a corresponds to the area enclosed in the white rectangle shown in the inset of Fig. 4b recorded using secondary electrons, whereas Fig. 4b corresponds to exactly the same area but recorded using backscattered electrons. As it is well-known, backscattered electrons are more sensitive to differences in the atomic weight of the elements present in the sample, which in our case means that the Au_3Cu metal nanoparticles are easy to identify as bright dots in the image with respect to the TiO_2 support. This is exactly what it is seen in Fig. 4b, where some of the metal nanoparticles are enclosed by white circles. A similar good dispersion of the metal nanoparticles on the titania support were observed for the other AuCu/TiO₂ samples, which means that the impregnation method used was successful in preparing photocatalysts decorated with individual Au_3Cu metal nanoparticles.

A complete microstructural characterization of the AuCu/TiO₂ photocatalysts was carried out by HRTEM. Fig. 5a and b show representative images of the outer part of the urchins in the AuCu/Ti-MU sample. The urchins are crystalline and the lattice fringes of the crystallites corresponded to rutile, as expected from XRD and Raman results. The surface of the rutile crystallites exhibited mainly the {110} planes at 3.2 Å (Fig. 5a). The metal nanoparticles appeared darker in the images because they showed strong electron diffraction and exhibited lattice fringes corresponding to Au_3Cu alloy (Fig. 5b). They

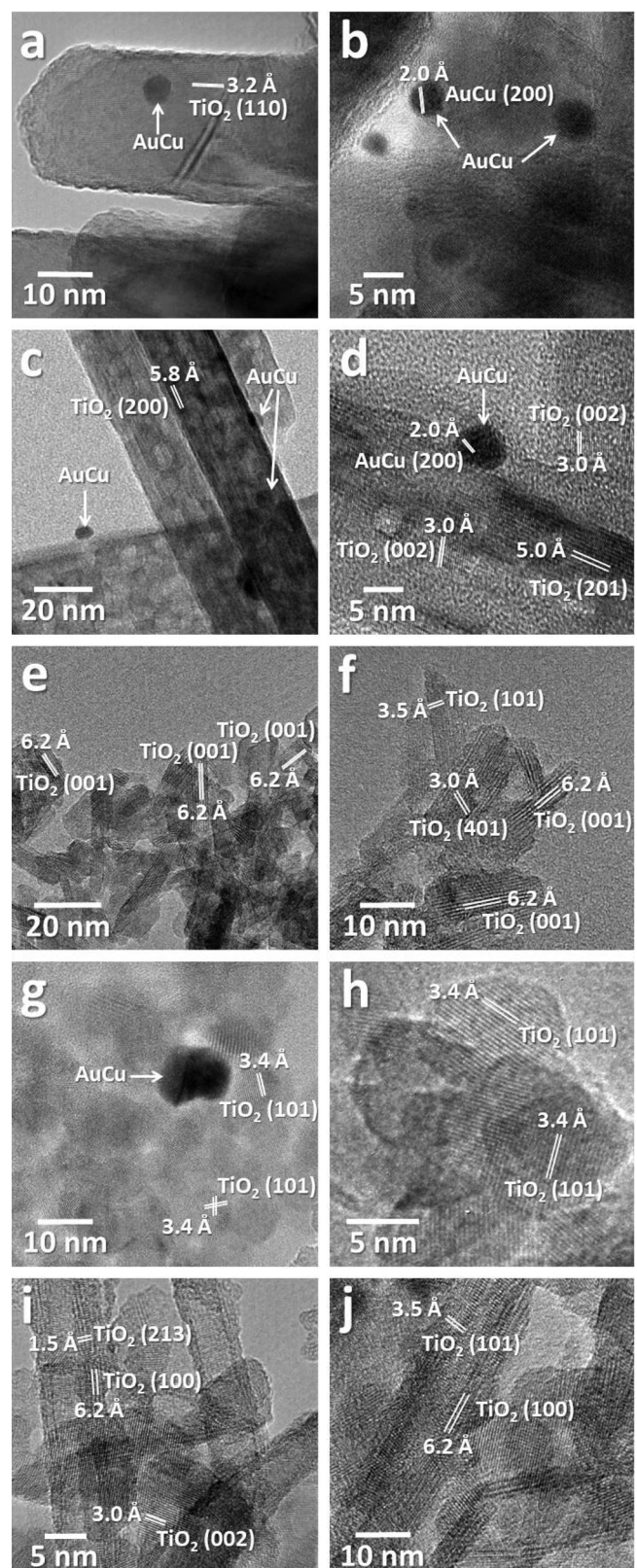


Fig. 5. HRTEM images of photocatalysts AuCu/Ti-MU (a,b), AuCu/Ti-NB (c,d), AuCu/Ti-NW (e,f), AuCu/Ti-MR (g,h) and AuCu/Ti-NT (i,j).

were rounded (with no developed facets) and their size was in the range 4–5 nm (Table 2), which is in accordance to the size growth expected after calcination at 573 K as reported previously [47]. The microstructure of the titania nanobelts was also totally crystalline and their

surface exposed almost exclusively the {200} planes at 5.8 Å of the TiO₂(B) polymorph (Fig. 5c). The HRTEM images also showed abundant regular voids inside the nanobelts as brighter areas, as described elsewhere for TiO₂(B) [58]. The titania nanobelts appeared decorated with well-dispersed and rounded Au₃Cu metal nanoparticles with a narrow size distribution centered at about 5 nm (Fig. 5c and d). The titania nanowires were also perfectly crystalline (Fig. 5e and f) and the main planes exposed at the surface belonged to the {001} family at 6.2 Å of the TiO₂(B) polymorph [59]. The microrods in the Ti-MR sample could not be studied by HRTEM because their thickness exceeded the maximum allowed value of thickness for electrons to be properly transmitted through the sample. However, HRTEM images were recorded at the corners of the microrods and the presence of titania nanoparticles measuring ca. 4–6 nm was unambiguously recognized, confirming previous SEM observations. The lattice fringes at 3.4 Å correspond to the (101) crystallographic planes of anatase (Fig. 5g and h). Finally, HRTEM allowed to confirm the structure of the titania nanotubes in AuCu/Ti-NT (Fig. 5h and i). As illustrated in the images, the nanotubes showed well-defined planes at the edges, whereas their central part appeared brighter, indicating the existence of a hollow structure. The nanotubes were aligned parallel to the (100) crystallographic planes of anatase at 6.2 Å. The size of the Au₃Cu metal nanoparticles was similar to those recorded over the other samples (Table 2) in accordance to the preparation method using preformed Au₃Cu alloy nanoparticles. Also, the metal loading was similar (Table 2).

The surface of the AuCu/TiO₂ photocatalysts was studied by XPS. In addition to adventitious carbon, the only detected signals came from the TiO₂ support and the Au₃Cu nanoparticles. In all cases, sodium and sulfur signals were absent, indicating that the surfaces of the photocatalysts were not contaminated with residual Na from NaOH used during the hydrothermal treatments and with S from the thiolate shells of the preformed Au₃Cu alloy nanoparticles. This observation is important since organic fragments at the surface of titania photocatalysts can act either as a recombination electron-hole centers or as promoters in the photogeneration of hydrogen [60]. The Ti 2p region recorded for each photocatalyst is shown in Fig. 6. In all cases the spectra were dominated by signals at 458.5 ± 0.2 eV (Ti 2p_{3/2}) and 464.2 ± 0.2 eV

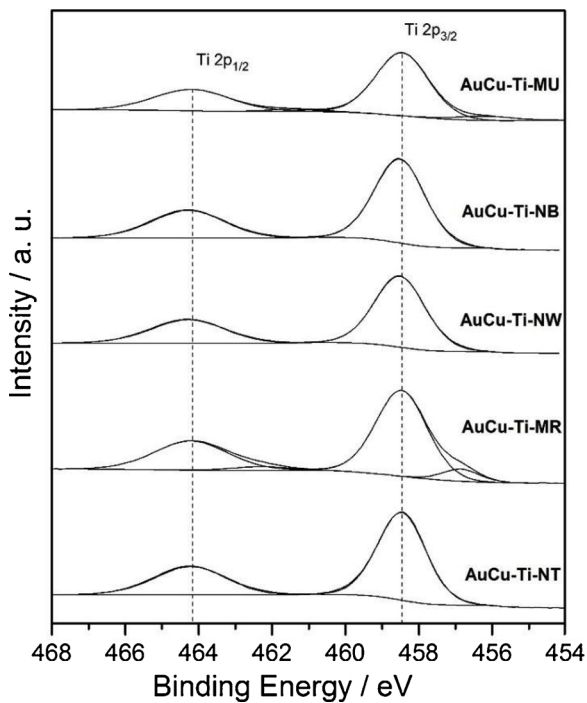


Fig. 6. Ti 2p XP spectra recorded over the AuCu/TiO₂ photocatalysts.

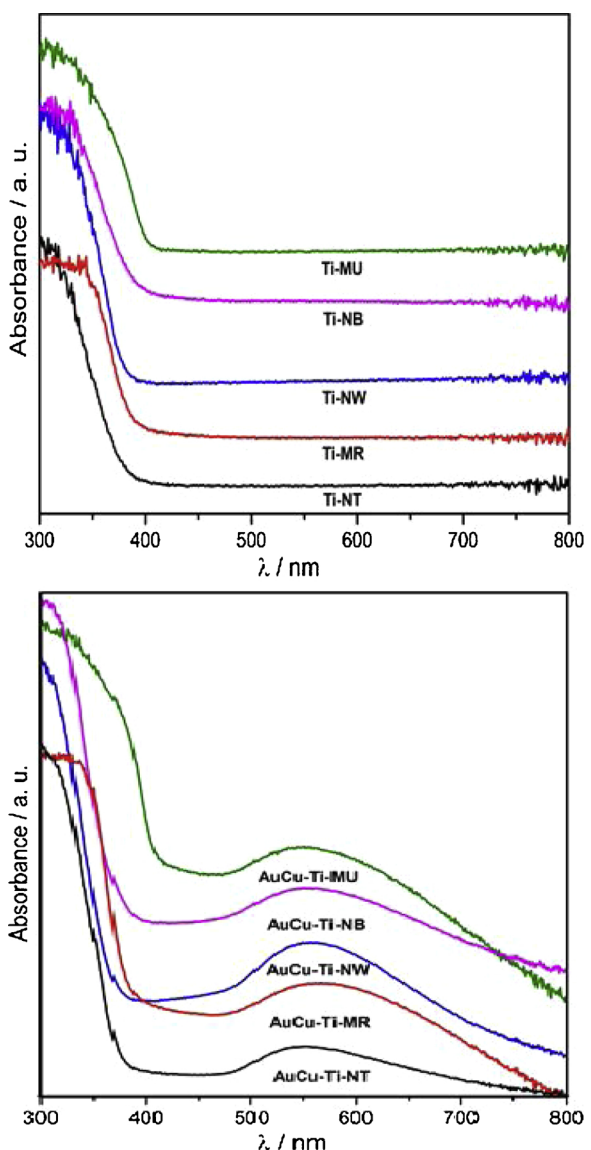


Fig. 7. UV-vis spectra recorded over the nanoshaped titania supports (a) and the AuCu/TiO₂ photocatalysts (b).

(Ti 2p_{1/2}) characteristic of Ti⁴⁺ in the TiO₂ structure (with a spin-orbit splitting of 5.7 eV). In the spectrum corresponding to the sample AuCu/Ti-MR, the existence of another doublet at 456.8 eV (Ti 2p_{3/2}) and 462.3 eV (Ti 2p_{1/2}) characteristic of Ti³⁺ was also observed [59,61]. This can be due to a stabilization effect of oxygen vacancies by small anatase nanoparticles of 4–6 nm at the surface of the microrods (Fig. 5h). Traces of Ti³⁺ were also detected in the spectrum of the sample AuCu/Ti-MU, but to a much lower extent. Fig. S1 shows the Au 4f spectra of the AuCu/TiO₂ photocatalysts. In all cases, the binding energies of Au 4f_{7/2} and Au 4f_{5/2} were at 84.3 ± 0.1 and 87.1 ± 0.1 eV, respectively, which indicated the presence of metallic Au in the AuCu nanoparticles deposited on all the nanoshaped titania supports. The spectra recorded in the Cu 2p region (Fig. S2) was quite noisy given the low concentration of Cu in the preformed nanoparticles, but the binding energies of Cu 2p_{3/2} and Cu 2p_{1/2} recorded at about 932.3 and 952.4 eV, respectively, and the absence of satellite lines were consistent with Cu being in metallic state in AuCu alloy [62]. As expected, the surface atomic Au/Cu ratio was similar for all samples at about 2.9 ± 0.3.

Fig. 7 shows the UV-vis absorption spectra of the nanoshaped titania supports (Fig. 7a) and the AuCu/TiO₂ photocatalysts (Fig. 7b).

The intense absorption feature at about 300–400 nm is characteristic of the O 2p-Ti 3d transition (from valence band to conduction band) of TiO₂, being the position of the absorption edge determined by the structural characteristics and polymorphism of titania. Table 2 compiles the band gap energies for each nanoshaped titania support obtained from Tauc plots. As expected, the band gap of the titania urchins, 3.06 eV, was clearly lower than those of the other nanoshapes because the titania urchins were composed exclusively by rutile, which exhibits a lower band gap [9]. The band gap of TiO₂(B) is about 0.1 eV lower than that of anatase [63], which explains the slight lower band gap energy recorded for sample Ti-NB with respect to Ti-NT and Ti-NW (3.31 vs. 3.32–3.34 eV). In contrast, titania microrods, which were constituted exclusively by anatase, showed a red shift of the absorption edge with respect to the other titania nanoshapes containing anatase, which resulted in a low band gap energy of 3.27 eV. This could be explained by the presence of small anatase nanoparticles of 4–6 nm decorating the titania microrods, as evidenced by HRTEM (Fig. 5h), since it has been reported that there is a dependency of anatase crystallite size on its optical properties; the smaller the particle size the smaller the band gap of anatase until the Bohr radius is reached [64]. The band gap energies of the titania nanoshapes were essentially unaltered after deposition of the preformed Au₃Cu metal nanoparticles (Fig. 7b), in accordance to similar studies on Au/TiO₂ photocatalysts [35].

As expected, after deposition of the preformed metal nanoparticles a new absorption band at 500–650 nm was observed due to the localized surface plasmon resonance (LSPR) of the Au₃Cu alloy nanoparticles. The band was rather broad, according to the presence of 4–6 nanometer-sized Au₃Cu nanoparticles [38]. In all samples except for AuCu/Ti-MR, the LSPR band was centred at 555 ± 3 nm, which is a direct demonstration that the photocatalysts contained Au₃Cu metal nanoparticles with a similar size, in accordance to HRTEM measurements (Table 2). However, the photocatalyst AuCu/Ti-MR exhibited a LSPR band at a higher wavelength, 567 nm, which pointed to the presence of larger Au₃Cu metal particles. This is also in accordance to HRTEM, which showed a mean Au₃Cu nanoparticle size larger than that of the other samples (5.8 vs. 4.6–5.0 nm, respectively).

3.2. Photocatalytic performance

Photocatalytic experiments can be strongly affected by mass transfer and photon delivery limitations [48]. For that reason it is very important to carry out preliminary experiments to define the testing conditions that will allow a proper comparison of the photocatalytic performance between the different samples. This procedure is particularly important when calculating apparent quantum efficiencies [65], [66]. A first set of experiments were carried out to study the photon transfer limitations in our continuous tubular photoreactor at a fixed contact time value of ca. 0.14 s by varying the amount of photocatalyst deposited in the membranes used under a constant irradiance of 82 mW cm⁻². As a representative example, Fig. 8 shows the normalized photocatalytic hydrogen rates ($\mu\text{mol H}_2 \text{ g}_{\text{cat}}^{-1} \text{ min}^{-1}$) obtained over the Ti-MR sample. It is clearly observed that the amount of catalyst should be in the 1–1.5 mg range for an optimum photon usage and that a larger quantity of photocatalyst resulted in a lower hydrogen photoproduction normalized rates than the 1–1.5 mg range. Similar results were obtained over the other titania nanoshaped supports and over the AuCu/TiO₂ samples. On the other hand, at a given photocatalyst loading, the contact time was varied between 0.07 and 0.28 s and we did not observe limitations of mass transfer in these conditions.

Both the nanoshaped titania supports and standard P25 as prepared and after decoration with preformed nanoparticles of Au-Cu alloy were tested at room temperature and atmospheric pressure for the photogeneration of hydrogen under dynamic conditions using a gaseous mixture of EtOH:H₂O = 1:9 (molar) at a gas hourly space velocity of GHSV = 26,000 h⁻¹ for 2 h. The only products obtained were hydrogen

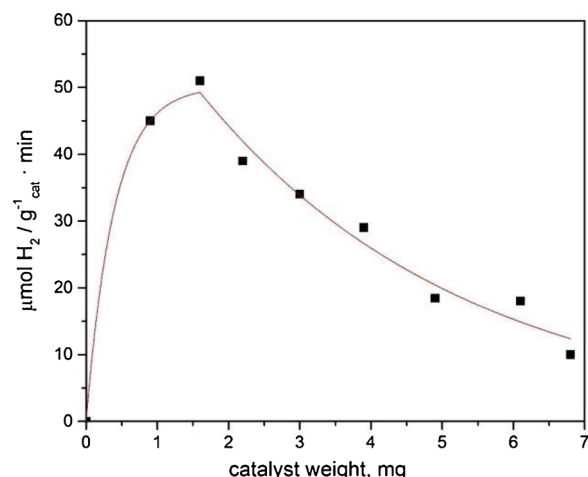


Fig. 8. Hydrogen photoproduction rates obtained over the Ti-MR sample at room temperature and atmospheric pressure in a tubular glass photoreactor operating under dynamic conditions. EtOH:H₂O = 1:9 (molar), GHSV = 26,000 h⁻¹, 82 mW cm⁻².

and acetaldehyde in equimolar amounts according to the well-known photodehydrogenation reaction of ethanol, $\text{C}_2\text{H}_5\text{OH} \rightarrow \text{CH}_3\text{CHO} + \text{H}_2$ [1]. Fig. 9 shows the hydrogen photoproduction rates obtained for each sample over time on stream.

It is important to highlight that all the samples exhibited a very stable photocatalytic generation of hydrogen except for AuCu/Ti-NT and AuCu/Ti-P25, which showed a progressive deactivation. This could be related to a strong adsorption of acetaldehyde on the surface of the photocatalysts, which in turn could inhibit the hole scavenging by ethanol molecules [67,68].

Fig. 10 shows the hydrogen photoproduction rates and apparent quantum efficiencies (AQE) values for each sample recorded after 2 h on stream. For the bare nanoshaped titania supports the photogeneration rate of hydrogen followed the trend Ti-NT > > Ti-MR ~ Ti-P25 > Ti-NW > Ti-NB > Ti-MU. It is interesting to note the higher photoactivity of the titania nanotubes, which are composed solely by anatase, than the standard P25 titania sample, where the coexistence of anatase and rutile has shown superior photocatalytic properties than pure anatase conventional nanoparticles. This can be due either to a higher number of surface photocatalytic sites due to the high surface area exhibited by Ti-NT with respect to Ti-P25 (274 vs. 47 m² g⁻¹, respectively), or to the nanotubular architecture, which has been reported to decrease the electron-hole recombination rate [69]. Also, titania microrods, which are constituted by anatase only, exhibited a similar hydrogen photoproduction rate than Ti-P25. In this case, the surface areas of both samples were similar (60 vs. 47 m² g⁻¹), which suggests that the microrod architecture was responsible for the relatively high photoactivity observed. In contrast, titania nanobelts and nanowires, in spite of their 1D architecture, showed lower hydrogen photoproduction rates. This can be ascribed to the presence of TiO₂(B), which has been reported to be less photoactive than anatase [70,71]. The titania microurchins showed the lowest hydrogen photogeneration rate due to the exclusive presence of rutile, which has the fastest electron-hole recombination rate. In this case the 1D architecture did not provide with additional advantages.

The addition of Au₃Cu alloy nanoparticles clearly promoted the photogeneration of hydrogen as expected [38,62] except for Ti-MU. The photoactivity of the different titania morphologies decorated with the Au₃Cu alloy nanoparticles followed the trend: AuCu/Ti-MR ~ AuCu/Ti-P25 > AuCu/Ti-NT > AuCu/Ti-NW > AuCu/Ti-NB > AuCu/Ti-MU. The promotion of the photogeneration of hydrogen was particularly significant for AuCu/Ti-MR and AuCu/Ti-P25 with respect to their respective Ti-MR and Ti-P25 supports (Fig. 10), although the

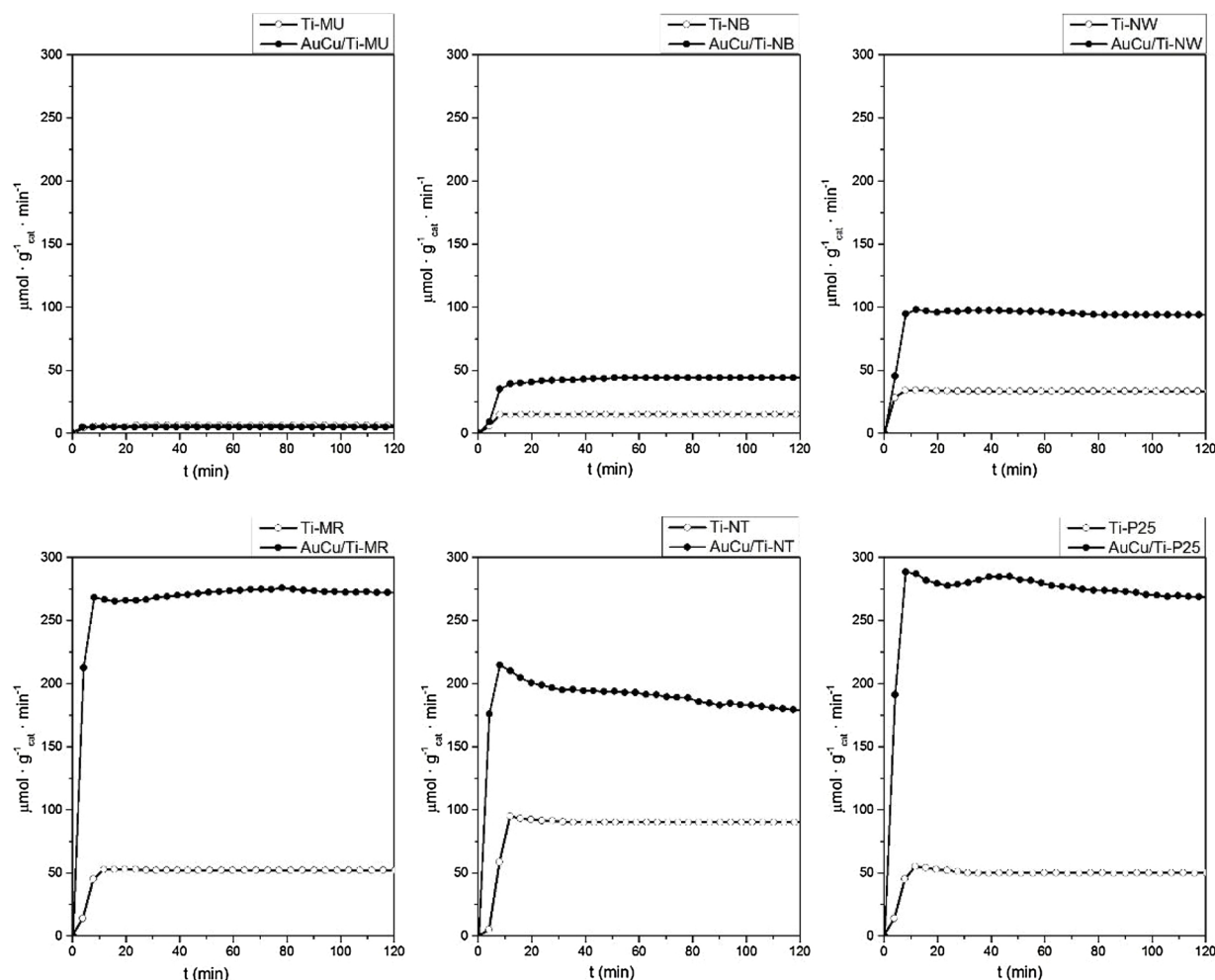


Fig. 9. Hydrogen photoproduction rates obtained over the titania nanoshaped supports and P25 and over the AuCu/TiO₂ photocatalysts over time on stream at room temperature and atmospheric pressure in a tubular glass photoreactor operating under dynamic conditions. EtOH:H₂O = 1:9 (molar), GHSV = 26,000 h⁻¹, 82 mW cm⁻².

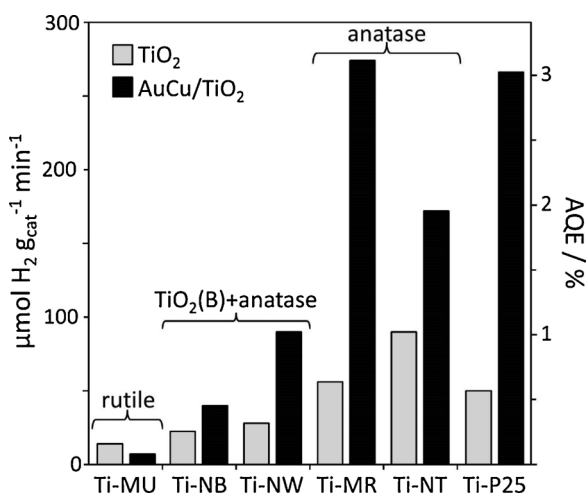


Fig. 10. Hydrogen photoproduction rates and apparent quantum efficiencies (AQEs) obtained over the titania nanoshaped supports and over the AuCu/TiO₂ photocatalysts after 2 h on stream in a tubular glass photoreactor operating under dynamic conditions. EtOH:H₂O = 1:9 (molar), GHSV = 26,000 h⁻¹, 82 mW cm⁻².

performance of AuCu/Ti-MR was clearly superior because, as pointed out earlier, the photoproduction rate of hydrogen obtained over AuCu/Ti-P25 decreased over time on stream (Fig. 9). The apparent quantum efficiency (AQE) for the photogeneration of hydrogen was calculated using the equation $\text{AQE} = (2 n_{\text{H}_2}/n_p) \times 100$, where n_{H_2} is the number of molecules of generated H₂ and n_p the number of incident photons reaching the catalyst [72]. The maximum AQE recorded was ca. 3.1% for AuCu/Ti-MR (Fig. 10).

It should be pointed out that the number and quality of contact points between the Au₃Cu alloy nanoparticles and the different titania supports was similar because, as discussed earlier, we used preformed nanoparticles of Au₃Cu alloy with the same characteristics. Therefore, it is possible to compare in a proper way the role of the titania morphology on the photoproduction of hydrogen after decorating the surface with the Au₃Cu nanoparticles. Taking into account that the hydrogen photogeneration rates of Ti-MR and Ti-P25 were very similar (50 vs. 52 μmol H₂ g⁻¹ min⁻¹) and those recorded for AuCu/Ti-MR and AuCu/Ti-P25 were also very similar (272 vs. 268 μmol H₂ g⁻¹ min⁻¹), it is likely that the enhancement of electron transport between the surface of titania microrods and of P25 and the Au₃Cu alloy nanoparticles follows a similar route. In contrast, the enhancement of hydrogen photoproduction over AuCu/Ti-NT was ca. only twice than that

of the Ti-NT support (176 vs. $90 \mu\text{mol H}_2 \text{g}^{-1} \text{min}^{-1}$, respectively), which could be an indication that a different electron transport mechanism takes place between the surface of titania nanotubes and AuCu alloy nanoparticles with respect to Ti-MR and Ti-P25, even if Ti-NT are constituted by anatase. The particular titania microrod architecture, therefore, can be considered to play a key role on the photogeneration of hydrogen. Finally, the photocatalytic performance of the AuCu/Ti-MR sample ($16.3 \text{ mmol H}_2 \text{g}^{-1} \text{h}^{-1}$) is significantly better compared with other M/TiO₂ systems reported in the literature operating under similar conditions [73,74]. In particular, Chen et al. reported hydrogen photoproduction rates of 11.6 and $10.3 \text{ mmol H}_2 \text{g}^{-1} \text{h}^{-1}$ in ethanol-water mixtures (10 vol% alcohol) for Ni/P25 TiO₂ and Au/P25 TiO₂, respectively [75].

4. Conclusions

A series of well-defined titania 1D architectures (tubes, wires, rods, belts and urchins) were synthesized, characterized and tested for the photogeneration of hydrogen under dynamic conditions and in gas phase from water-ethanol mixtures and their photocatalytic performances were compared with a standard TiO₂ P25 sample. The hydrogen photoproduction rates normalized on a weight basis followed the trend:

nanotubes > microrods ~ P25 > nanowires > nanobelts
> microurchins

The good results obtained over titania nanotubes could be due to a higher number of surface photocatalytic sites than the other samples, due to its high surface area ($275 \text{ m}^2 \text{ g}^{-1}$), or to the nanotubular architecture, which exhibits a low electron-hole recombination rate. The anatase morphologies (nanotubes and microrods) were superior to the samples containing the TiO₂(B) polymorph (nanowires and nanobelts) and rutile (microurchins). These titania 1D structures were decorated with the same amount of Au₃Cu alloy nanoparticles and the photoproduction of hydrogen was strongly enhanced, but to a different degree depending on the architecture of the titania support considered. The hydrogen photoproduction rates normalized on a weight basis followed the trend:

AuCu/microrods ~ AuCu/P25 > AuCu/nanotubes >

AuCu/nanowires > AuCu/nanobelts > AuCu/microurchins

The strong enhancement of the photogeneration of hydrogen over the titania microrods decorated with AuCu alloy nanoparticles merits to be highlighted. In addition, the photoproduction of hydrogen exhibited by this sample was very stable, whereas the standard TiO₂ P25 sample decorated with Au₃Cu nanoparticles suffered a progressive deactivation during time on stream.

Acknowledgments

This work has been funded by projects MINECO/FEDER ENE2015-63969-R and GC 2017 SGR 128. JL is a Serra Húnter Fellow and is grateful to ICREA Academia program. LM is grateful to CONACYT México for the PhD grant no. 409809.

Appendix A. Supplementary data

Supplementary material related to this article can be found, in the online version, at doi:<https://doi.org/10.1016/j.apcatb.2019.02.053>.

References

- [1] M. Murdoch, G.I.N. Waterhouse, M.A. Nadeem, J.B. Metson, M.A. Keane, R.F. Howe, J. Llorca, H. Idriss, The effect of gold loading and particle size on photocatalytic hydrogen production from ethanol over Au/TiO₂ nanoparticles, *Nat. Chem.* 3 (2011) 489–492.
- [2] Y. Ma, X. Wang, Y. Jia, X. Chen, H. Han, C. Li, Titanium dioxide-based nanomaterials for photocatalytic fuel generations, *Chem. Rev.* 114 (2014) 9987–10043.
- [3] Slamet D. Tristantini, Valentina M. Ibadurrohman, Photocatalytic hydrogen production from glycerol-water mixture over Pt-N-TiO₂ nanotube photocatalyst, *Int. J. Energy Res.* 37 (2013) 1372–1381.
- [4] S. Sun, P. Gao, Y. Yang, P. Yang, Y. Chen, Y. Wang, N-doped TiO₂ nanobelts with coexposed (001) and (101) facets and their highly efficient visible-light-driven photocatalytic hydrogen production, *ACS Appl. Mater. Interfaces* 8 (2016) 18126–18131.
- [5] X. Wang, Z. Li, J. Shi, Y. Yu, One-dimensional titanium dioxide nanomaterials: nanowires, nanorods, and nanobelts, *Chem. Rev.* 114 (2014) 9346–9384.
- [6] A.G. Dosado, W.-T. Chen, A. Chan, D. Sun-Waterhouse, G.I.N. Waterhouse, Novel Au/TiO₂ photocatalysts for hydrogen production in alcohol-water mixtures based on hydrogen titanate nanotube precursors, *J. Catal.* 330 (2015) 238–254.
- [7] B.A. Aragaw, C.-J. Pan, W.-N. Su, H.-M. Chen, J. Rick, B.-J. Hwang, Facile one-pot controlled synthesis of Sn and C codoped single crystal TiO₂ nanowire arrays for highly efficient photoelectrochemical water splitting, *Appl. Catal. B Environ.* 163 (2015) 478–486.
- [8] J. Cai, Y. Wang, Y. Zhu, M. Wu, H. Zhang, X. Li, Z. Jiang, M. Meng, In situ formation of disorder-engineered TiO₂(B)-anatase heterophase junction for enhanced photocatalytic hydrogen evolution, *ACS Appl. Mater. Interfaces* 7 (2015) 24987–24992.
- [9] T.-D. Nguyen-Phan, S. Luo, D. Vovchok, J. Llorca, S. Sallis, S. Kattel, W. Xu, L.F.J. Piper, D.E. Polyansky, S.D. Senanayake, D.J. Stacchiola, J.A. Rodriguez, Three-dimensional ruthenium-doped TiO₂ sea urchins for enhanced visible-light-responsive H₂ production, *Phys. Chem. Chem. Phys.* 18 (2016) 15972–15979.
- [10] A. Meng, J. Zhang, D. Xu, B. Cheng, J. Yu, Enhanced photocatalytic H₂-production activity of anatase TiO₂ nanosheet by selectively depositing dual-cocatalysts on {101} and {001} facets, *Appl. Catal. B Environ.* 198 (2016) 286–294.
- [11] S. Li, G. Zhang, D. Guo, L. Yu, W. Zhang, Anodization fabrication of highly ordered TiO₂ nanotubes, *J. Phys. Chem. C* 113 (2009) 12759–12765.
- [12] R. Liu, W.D. Yang, L.S. Qiang, J.F. Wu, Fabrication of TiO₂ nanotube arrays by electrochemical anodization in an NH₄F/H₃PO₄ electrolyte, *Thin Solid Films* 519 (2011) 6459–6466.
- [13] B.-X. Lei, Q.-P. Luo, Z.-F. Sun, D.-B. Kuang, C.-Y. Su, Fabrication of partially crystalline TiO₂ nanotube arrays using 1,2-propanediol electrolytes and application in dye-sensitized solar cells, *Adv. Powder Technol.* 24 (2013) 175–182.
- [14] H. Shin, D.K. Jeong, J. Lee, M.M. Sung, J. Kim, Formation of TiO₂ and ZrO₂ nanotubes using atomic layer deposition with ultraprecise control of the wall thickness, *Adv. Mater.* 16 (2004) 1197–1200.
- [15] V.G. Pol, Y. Langzam, A. Zaban, Application of microwave superheating for the synthesis of TiO₂ rods, *Langmuir* 23 (2007) 11211–11216.
- [16] Y. Yang, G. Wang, Q. Deng, D.H.L. Ng, H. Zhao, Microwave-assisted fabrication of nanoparticulate TiO₂ microspheres for synergistic photocatalytic removal of Cr(VI) and methyl orange, *ACS Appl. Mater. Interfaces* 6 (2014) 3008–3015.
- [17] J. Liu, Y. Hu, F. Gu, C. Li, Flame synthesis of ball-in-shell structured TiO₂ nanospheres, *Ind. Eng. Chem. Res.* 48 (2009) 735–739.
- [18] H. Li, Z. Bian, J. Zhu, D. Zhang, G. Li, Y. Huo, H. Li, Y. Lu, Mesoporous titania spheres with tunable chamber structure and enhanced photocatalytic activity, *J. Am. Chem. Soc.* 129 (2007) 8406–8407.
- [19] L. Xiang, S. Liu, J. Yin, X. Zhao, Bimetallic core/shell nanoparticle-decorated 3D urchin-like hierarchical TiO₂ nanostructures with magneto-responsive and decolorization characteristics, *Nanoscale Res. Lett.* 10 (2015) 84.
- [20] M. Fathy, H. Hamad, A.E.H. Kashyout, Influence of calcination temperatures on the formation of anatase TiO₂ nanorods with a polyol-mediated solvothermal method, *RSC Adv.* 6 (2016) 7310–7316.
- [21] L. Xiang, X. Zhao, J. Yin, B. Fan, Well-organized 3D urchin-like hierarchical TiO₂ microspheres with high photocatalytic activity, *J. Mater. Sci.* 47 (2012) 1436–1445.
- [22] S. Liu, J. Yu, M. Jaroniec, Tunable photocatalytic selectivity of hollow TiO₂ microspheres composed of anatase polyhedra with exposed {001} facets, *J. Am. Chem. Soc.* 132 (2010) 11914–11916.
- [23] F. Jiang, S. Zheng, L. An, H. Chen, Effect of calcination temperature on the adsorption and photocatalytic activity of hydrothermally synthesized TiO₂ nanotubes, *Appl. Surf. Sci.* 258 (2012) 7188–7194.
- [24] L.-Q. Weng, S.-H. Song, S. Hodgson, A. Baker, J. Yu, Synthesis and characterisation of nanotubular titanates and titania, *J. Eur. Ceram. Soc.* 26 (2006) 1405–1409.
- [25] S. Sreekantan, L.C. Wei, Study on the formation and photocatalytic activity of titanate nanotubes synthesized via hydrothermal method, *J. Alloys Compd.* 490 (2010) 436–442.
- [26] M. Alam Khan, Hee-Tae Jung, O.-Bong Yang, Synthesis and characterization of ultrahigh crystalline TiO₂ nanotubes, *J. Phys. Chem. B* 110 (2006) 6626–6630.
- [27] M.-C. Wu, P.-Y. Wu, T.-H. Lin, T.-F. Lin, Photocatalytic performance of Cu-doped TiO₂ nanofibers treated by the hydrothermal synthesis and air-thermal treatment, *Appl. Surf. Sci.* 430 (2018) 390–398.
- [28] E.M. Neville, J.M.D. MacElroy, K.R. Thampi, J.A. Sullivan, Visible light active C-doped titanate nanotubes prepared via alkaline hydrothermal treatment of C-doped nanoparticulate TiO₂: photo-electrochemical and photocatalytic properties, *J. Photochem. Photobiol. A: Chem.* 267 (2013) 17–24.
- [29] C. Anastasescu, S. Mihaiu, S. Preda, M. Zaharescu, 1D Oxide Nanostructures Obtained by Sol-Gel and Hydrothermal Methods, Springer International Publishing, 2016, pp. 5–75.
- [30] S.K. Gupta, A. Sharma, A.K. Garg, Synthesis processes, characterization methods and energy related applications of nano-crystalline titanium dioxide, in: K.Y. Cheong (Ed.), Two-Dimensional Nanostructures for Energy-Related Applications, CRC Press, Boca Raton, Florida, 2017, pp. 269–295.
- [31] M. Ge, J. Cai, J. Ioccocia, C. Cao, J. Huang, X. Zhang, J. Shen, S. Wang, S. Zhang, K.-Q. Zhang, Y. Lai, Z. Lin, A review of TiO₂ nanostructured catalysts for sustainable

H₂ generation, *Int. J. Hydrogen Energy* 42 (2017) 8418–8449.

[32] M.D. Hernández-Alonso, S. García-Rodríguez, B. Sánchez, J.M. Coronado, Revisiting the hydrothermal synthesis of titanate nanotubes: new insights on the key factors affecting the morphology, *Nanoscale* 3 (2011) 2233–2240.

[33] M.Á. López Zavala, S.A. Lozano Morales, M. Ávila-Santos, Synthesis of stable TiO₂ nanotubes: effect of hydrothermal treatment, acid washing and annealing temperature, *Heliyon* 3 (2017) 1–18.

[34] P. Shen, S. Zhao, D. Su, Y. Li, A. Orlov, Outstanding activity of sub-nm Au clusters for photocatalytic hydrogen production, *Appl. Catal. B Environ.* 126 (2012) 153–160.

[35] L. Martínez, M. Benito, I. Mata, L. Soler, E. Molins, J. Llorca, Preparation and photocatalytic activity of Au/TiO₂ lyogels for hydrogen production, *Sustain. Energy Fuels* 2 (2018) 2284–2295.

[36] Z. Jiang, M.A. Isaacs, Z.W. Huang, W. Shangguan, Y. Deng, A.F. Lee, Active site elucidation and optimization in Pt Co-catalysts for photocatalytic hydrogen production over titania, *ChemCatChem* 9 (2017) 4268–4274.

[37] L. Soler, A. Casanovas, A. Urrich, I. Angurell, J. Llorca, CO oxidation and COPrOx over preformed Au nanoparticles supported over nanoshaped CeO₂, *Appl. Catal. B Environ.* 197 (2016) 47–55.

[38] E. Bonmatí, A. Casanovas, I. Angurell, J. Llorca, Hydrogen photoproduction from ethanol-water mixtures over Au-Cu alloy nanoparticles supported on TiO₂, *Top. Catal.* 58 (2015) 77–84.

[39] W. Chen, Y. Wang, S. Liu, L. Gao, L. Mao, Z. Fan, W. Shangguan, Z. Jiang, Non-noble metal Cu as a cocatalyst on TiO₂ nanorod for highly efficient photocatalytic hydrogen production, *Appl. Surf. Sci.* 445 (2018) 527–534.

[40] Z. He, J. Fu, B. Cheng, J. Yu, S. Cao, Cu₂(OH)₂CO₃ clusters: novel noble-metal-free cocatalysts for efficient photocatalytic hydrogen production from water splitting, *Appl. Catal. B Environ.* 205 (2017) 104–111.

[41] T. Kasuga, M. Hiramatsu, A. Hoson, T. Sekino, K. Niihara, Formation of titanium oxide nanotube, *Langmuir* 14 (1998) 3160–3163.

[42] T. Lan, Y. Liu, J. Dou, Z. Hong, M. Wei, Hierarchically porous TiO₂ microspheres as a high performance anode for lithium-ion batteries, *J. Mater. Chem. A Mater. Energy Sustain.* 2 (2014) 1102–1106.

[43] Q. Li, B. Liu, Y. Li, R. Liu, X. Li, D. Li, S. Yu, D. Liu, P. Wang, B. Li, B. Zou, T. Cui, G. Zou, Ethylene glycol-mediated synthesis of nanoporous anatase TiO₂ rods and rutile TiO₂ self-assembly chrysanthemums, *J. Alloys Compd.* 471 (2009) 477–480.

[44] M. Brust, M. Walker, D. Bethell, D.J. Schiffrin, R. Whymann, Synthesis of thiol-derivatised gold nanoparticles in a two-phase liquid–liquid system, *J. Chem. Soc., Chem. Commun.* 0 (1994) 801–802.

[45] C.J. Kiely, J. Fink, J.G. Zheng, M. Brust, D. Bethell, D.J. Schiffrin, Ordered colloidal nanoalloys, *Adv. Mater.* 12 (2000) 640–643.

[46] M.J. Hostetler, C.J. Zhong, B.K.H. Yen, J. Anderegg, S.M. Gross, N.D. Evans, M. Porter, R.W. Murray, Stable, monolayer-protected metal alloy clusters, *J. Am. Chem. Soc.* 120 (1998) 9396–9397.

[47] J. Llorca, M. Domínguez, C. Ledesma, R.J. Chimentão, F. Medina, J. Sueiras, I. Angurell, M. Seco, O. Rossell, Propene epoxidation over TiO₂-supported Au–Cu alloy catalysts prepared from thiol-capped nanoparticles, *J. Catal.* 258 (2008) 187–198.

[48] E. Taboada, I. Angurell, J. Llorca, Dynamic photocatalytic hydrogen production from ethanol-water mixtures in an optical fiber honeycomb reactor loaded with Au/TiO₂, *J. Catal.* 309 (2014) 460–467.

[49] E. Molins, M.M. Benito, I. Mata, L. Martínez, L. Soler, J. Llorca, Au/TiO₂ lyogels for hydrogen production, *MRS Adv.* 2 (2017) 3499–3504.

[50] K.C. Sun, M.B. Qadir, S.H. Jeong, Hydrothermal synthesis of TiO₂ nanotubes and their application as an over-layer for dye-sensitized solar cells, *RSC Adv.* 4 (2014) 23223–23230.

[51] B. Liu, A. Khare, E.S. Aydil, TiO₂–B/anatase core–shell heterojunction nanowires for photocatalysis, *ACS Appl. Mater. Interfaces* 3 (2011) 4444–4450.

[52] W. Zhou, L. Gai, P. Hu, J. Cui, X. Liu, D. Wang, G. Li, H. Jiang, D. Liu, H. Liu, J. Wang, Phase transformation of TiO₂ nanobelts and TiO₂(B)/anatase interface heterostructure nanobelts with enhanced photocatalytic activity, *CrystEngComm.* 13 (2011) 6643–6649.

[53] J. Yan, G. Wu, N. Guan, L. Li, Z. Li, X. Cao, Understanding the effect of surface/bulk defects on the photocatalytic activity of TiO₂: anatase versus rutile, *Phys. Chem. Chem. Phys.* 15 (2013) 10978–10988.

[54] T. Ohsaka, Temperature dependence of the raman Spectrum in anatase TiO₂, *J. Phys. Soc. Japan.* 48 (1980) 1661–1668.

[55] S.K. Shahi, N. Kaur, V. Singh, Fabrication of phase and morphology controlled pure rutile and rutile/anatase TiO₂ nanostructures in functional ionic liquid/water, *Appl. Surf. Sci.* 360 (2016) 953–960.

[56] D. Praveen Kumar, N. Lakshmana Reddy, M. Mamatha Kumari, B. Srinivas, V. Durga Kumari, B. Sreedhar, V. Roddatis, O. Bondarchuk, M. Karthik, B. Neppolian, M.V. Shankar, Cu₂O-sensitized TiO₂ nanorods with nanocavities for highly efficient photocatalytic hydrogen production under solar irradiation, *Sol. Energy Mater. Sol. Cells* 136 (2015) 157–166.

[57] T. Beuvier, M. Richard-Plouet, L. Brohan, Accurate methods for quantifying the relative ratio of anatase and TiO₂(B) nanoparticles, *J. Phys. Chem. C.* 113 (2009) 13703–13706.

[58] Geng Wang, Qiang Wang, Lu Wu, J. Li, Photoelectrochemical study on charge transfer properties of TiO₂–B nanowires with an application as humidity sensors, *J. Phys. Chem. B* 110 (2006) 22029–22034.

[59] Y. Zhang, Z. Xing, X. Liu, Z. Li, X. Wu, J. Jiang, M. Li, Q. Zhu, W. Zhou, Ti³⁺ self-doped blue TiO₂(B) single-crystalline nanorods for efficient solar-driven photocatalytic performance, *ACS Appl. Mater. Interfaces* 8 (2016) 26851–26859.

[60] E. Aguiló, L. Soler, A. Casanovas, A.J. Moro, J.C. Lima, L. Rodríguez, J. Llorca, Gold (I)-complex-titania hybrid photocatalyst for hydrogen production, *ChemCatChem* 9 (2017) 3289–3292.

[61] H. Khan, I.K. Swati, Fe³⁺-doped anatase TiO₂ with d–d transition, oxygen vacancies and Ti³⁺ centers: synthesis, characterization, UV–vis photocatalytic and mechanistic studies, *Ind. Eng. Chem. Res.* 55 (2016) 6619–6633.

[62] M. Liu, W. Zhou, T. Wang, D. Wang, L. Liu, J. Ye, High performance Au–Cu alloy for enhanced visible-light water splitting driven by coinage metals, *Chem. Commun.* 52 (2016) 4694–4697.

[63] D. Yang, H. Liu, Z. Zheng, Y. Yuan, J. Zhao, E.R. Waclawik, X. Ke, H. Zhu, An efficient photocatalyst structure: TiO₂(B) nanofibers with a shell of anatase nanocrystals, *J. Am. Chem. Soc.* 131 (2009) 17885–17893.

[64] H. Lin, C.P. Huang, W. Li, C. Ni, S.I. Shah, Y.-H. Tseng, Size dependency of nanocrystalline TiO₂ on its optical property and photocatalytic reactivity exemplified by 2-chlorophenol, *Appl. Catal. B Environ.* 68 (2006) 1–11.

[65] T. Maschmeyer, M. Che, Catalytic aspects of light-induced hydrogen generation in water with TiO₂ and other photocatalysts: a simple and practical way towards a normalization? *Angew. Chem. Int. Ed.* 49 (2010) 1536–1539.

[66] H. Kisch, On the problem of comparing rates or apparent quantum yields in heterogeneous photocatalysis, *Angew. Chem. Int. Ed.* 49 (2010) 9588–9589.

[67] A. Castedo, A. Casanovas, I. Angurell, L. Soler, J. Llorca, Effect of temperature on the gas-phase photocatalytic H₂ generation using microreactors under UVA and sunlight irradiation, *Fuel* 222 (2018) 327–333.

[68] D. Finkelstein-Shapiro, A.M. Buchbinder, B. Vijayan, K. Bhattacharyya, E. Weitz, F.M. Geiger, K.A. Gray, Identification of binding sites for acetaldehyde adsorption on titania nanorod surfaces using CIMS, *Langmuir* 27 (2011) 14842–14848.

[69] G.K. Mor, K. Shankar, M. Paulose, O.K. Varghese, C.A. Grimes, Enhanced Photocleavage of Water Using Titania Nanotube Arrays 5 (2004), pp. 191–195.

[70] G. Xiang, T. Li, J. Zhuang, X. Wang, Large-scale synthesis of metastable TiO₂(B) nanosheets with atomic thickness and their photocatalytic properties, *Chem. Commun.* 46 (2010) 6801–6808.

[71] D. Yang, H. Liu, Z. Zheng, Y. Yuan, J. Zhao, E.R. Waclawik, X. Ke, H. Zhu, An efficient photocatalyst structure: TiO₂(B) nanofibers with a shell of anatase nanocrystals, *J. Am. Chem. Soc.* 131 (2009) 17885–17893.

[72] A. May-Masnou, L. Soler, M. Torras, P. Salles, J. Llorca, A. Roig, Fast and Simple microwave synthesis of TiO₂/Au nanoparticles for gas-phase photocatalytic hydrogen generation, *Front. Chem.* 6 (2018) 1–13.

[73] V. Kumaravel, S. Mathew, J. Barlett, S.C. Pillai, Photocatalytic hydrogen production using metal doped TiO₂: a review of recent advances, *Appl. Catal. B Environ.* 224 (2019) 1021–1064.

[74] N. Fajrina, M. Tahir, A critical review in strategies to improve photocatalytic water splitting towards hydrogen production, *Int. J. Hydrogen Energy* 44 (2019) 540–577.

[75] W.T. Chen, A. Chan, D. Sun, J. Llorca, H. Idriss, G.I.N. Waterhouse, Performance comparison of Ni/TiO₂ and Au/TiO₂ photocatalysts for H₂ production in different alcohol–water mixtures, *J. Catal.* 367 (2018) 27–42.